Volume 21
Number 43
21 November 2025
Pages 8245–8390

Soft Matter

rsc.li/soft-matter-journal

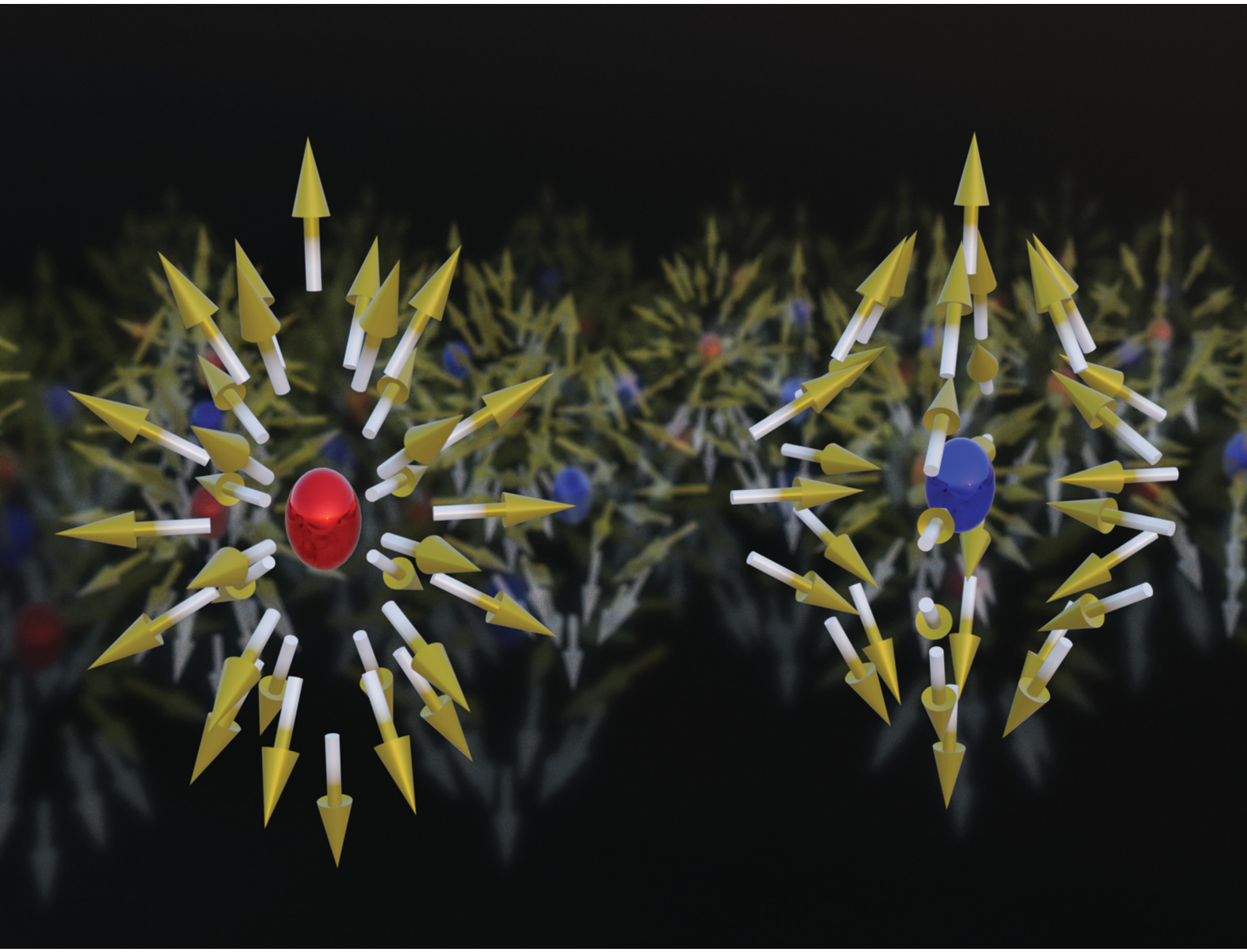

ISSN 1744-6848

ROYAL SOCIETY OF CHEMISTRY

PAPER
Natalia Podoliak *et al.*
Tunable defect patterns induced by a low-frequency electric field in ferroelectric nematic liquid crystals

20 YEARS ANNIVERSARY

Soft Matter

PAPER

View Article Online
View Journal | View Issue

Cite this: *Soft Matter*, 2025, **21**, 8257

Tunable defect patterns induced by a low-frequency electric field in ferroelectric nematic liquid crystals

Natalia Podoliak,* Lubor Lejček, Martin Cigl and Vladimíra Novotná

The regulation of topological structures and pattern formation has attracted wide attention in the field of condensed matter. Liquid crystals (LCs), as a class of soft matter, uniquely combine fluidity with anisotropic properties, making them ideal systems for exploring defect dynamics. When confined systems are subjected to external stimuli, LCs can exhibit a variety of topological defects. The recent discovery of ferroelectric nematics (N_F), characterized by high permittivity and spontaneous polarization, has opened new possibilities for technological applications, enriching the landscape of accessible topological phenomena. In this study, we demonstrate the formation of tunable two-dimensional arrays of topological defects in an N_F compound, induced by an alternating electric field in sandwich cells without pre-patterning. These defects self-organize into pseudo-square lattices, with their character and periodicity governed primarily by the frequency of the applied field and, to a lesser extent, by the cell thickness. We attribute the emergence of these structures to the interplay between elastic and electric forces appearing as a result of polar molecular reorientation. Our findings offer a promising approach for generating reconfigurable, spatially periodic polarization patterns, with potential relevance to future soft-matter-based devices and tunable photonic systems.

Received 22nd July 2025,
Accepted 24th August 2025

DOI: 10.1039/d5sm00747j

rsc.li/soft-matter-journal

1. Introduction

The regulation of topological structures and pattern formation has attracted wide attention in the fields of condensed matter and materials science.[1] In the solid state, topological insulators have promising applications in spintronic devices,[2] quantum computers,[3] and advanced magnetoelectronic and optical devices.[4] Topological soft matter opens new perspectives towards modern technologies due to interconnections between self-assembly and geometry.[5,6] Liquid crystals (LCs) as a self-assembly of organic molecules are known for their remarkable combination of fluidity and anisotropic properties. As a result of intermolecular interactions, thermotropic LCs can be organised in various phases within specific temperature ranges and sensitively reflect any external fields and conditions.

The behaviour of LC systems primarily depends on the confinement conditions and various kinds of defects can occur. For liquid crystal research, sandwich cells are utilised for electro-optical measurements. Such cells are made of two parallel glass plates with transparent conductive electrodes to apply an electric field across the cell. The orientation of the molecules and polarization in the cell are affected by the molecular alignment at the surfaces. Two basic configurations can be realised *via* a surfactant layer at the glass surfaces: planar alignment with a preferred parallel molecular orientation (rubbing direction) ensures the homogeneous geometry (HG); in the homeotropic geometry (HT), the molecules are arranged perpendicular to the surfaces.

Generally, all LC systems are prone to defect formation within their structure. In the homogeneous state, defects are not stable and tend to annihilate and minimise the free energy of the system. However, in the confined geometry, topological defects arise naturally due to the discontinuity of ordering at the surfaces. Disclination lines are present in nematics if the director makes continuous rotation along a closed loop. Previously, formation of 2D defect structures in a sample with one free surface under the influence of a magnetic field was described by De Gennes.[7] As defects can be observed in specific geometries with different upper and lower surfaces, a regular network of singular points was observed at the nematic–isotropic interface,[8] resulting in an oblique director orientation. Additionally, defect arrays can be induced by external stimuli. For example, an appearance of a chiral stripe pattern was induced in an achiral material by subjecting it to a pressure-driven flow in a microfluidic cell.[9] The possibility to influence the molecular orientation by the electric field and pattern formation is highly advantageous and challenging.[10,11] The

Institute of Physics of the Czech Academy of Sciences, Na Slovance 1999/2, 182 00 Prague 8, Czech Republic. E-mail: podoliak@fzu.cz

appearance of 2D periodic patterns under the influence of an AC electric field was reported for a nematic liquid crystal in the planar geometry.[12] Large-scale topological defect networks were induced by an AC electric field using an optical tweezers technique in a nematic liquid crystal doped with ionic impurities.[13] Additionally, arrays of micropillars modifying the cell surface were utilised for pattern stabilisation.[14] The above-mentioned topological structures appear due to system frustration and under very specific conditions, with limited control of parameters. A different mechanism is related to orientationally pre-patterned surfaces,[15] which depends on the advanced technology of photopatterning. However, the parameters of the pre-patterned configurations cannot be tuned.

Recently, a ferroelectric nematic phase (N_F) was experimentally realized,[16–18] a century after its prediction.[19,20] In the classical nematic phase (N), which can appear below the isotropic liquid (Iso) phase on cooling, there is a long-range orientational ordering with the prevailing molecular orientation described by a unit vector named director, n, having an inversion symmetry. In the N_F phase, the director represents an axial polar vector, and the head-to-tail symmetry is broken. Consequently, the resulting phase is polar, with spontaneous polarization being locally parallel to n. Since the N_F phase discovery, ferroelectric nematogens have been intensively studied.[21–31] For these materials, very large values of polarization as well as electric susceptibility have been confirmed.[21–27,32,33] Additionally, non-linear properties, namely, efficient second harmonic generation (SHG) supporting the polar character of the N_F phase, and an electro-optic response with exceptionally low threshold values have been reported,[25,34–36] giving these materials huge application potential.

A periodic polarization structure in a photopatterned sample was reported for ferroelectric nematics, giving a deeper insight into the flexoelectric coupling in the director field for such materials.[37] Recently, a square-lattice pattern structure was reported for the N_F material in planar geometry,[38] under a high-frequency electric field above Fréedericksz transition.

In this study, we demonstrate the possibility to create tunable 2D reconfigurable topological structures in ferroelectric nematics confined in simple sandwich cells without any pre-patterning, by the application of an AC electric field. The induced defects form pseudo-square lattices, which partially persist after the applied field is switched off. The periodicity of the structure can be changed by varying the field characteristics (frequency). We investigate the behaviour of the defect structures depending on the cell parameters and the applied electric field characteristics. We propose a theoretical explanation based on the competition between the elastic and electrical forces. Our findings could be useful for the design of patterns with reconfigurable spatially periodic polarization structures.

2. The pattern generation and observation

For the current investigation, a ferroelectric nematic material designated NF6 is utilised, exhibiting a direct transition from the Iso to N_F phase at 65 °C. The synthesis and mesomorphic characteristics of the material were published previously.[24] The studied material was filled into commercial glass cells, with transparent indium tin oxide (ITO) electrodes and surfactant layers ensuring the homeotropic geometry. The low-frequency electric field (1–500 Hz) with a sinusoidal or triangular profile was applied to the sample perpendicular to the surfaces and, hence, along the molecular long axis in this geometry.

The virgin texture observed under a polarized light optical microscope (POM) for a 5-μm HT sample in the N_F phase after cooling from Iso is shown in Fig. S1 in the SI. The texture contains a random distribution of small, coloured domains of irregular shapes, missing any periodic features, and its interpretation is problematic. After the application of an AC electric field, a periodic array of defects was induced. The pattern covered the whole electrode area, with inhomogeneities close to the electrode edges, as shown in Fig. 1(a). After switching off the field, the pattern persisted for some time, depending on the temperature at which the sample was held and, hence, the material viscosity. At room temperature (RT), the pattern did not disappear until the next day. However, it became smashed and contained additional smaller domains within the initial pattern (Fig. S2). For higher temperature and lower material viscosity, pattern degeneration was faster. In Fig. 1(b–d), one can see the evolution of the pattern with time for $T = 40$ °C, with the gradual appearance of the additional defects within the initial structure and the pattern degradation as a result.

We analysed the textures for various frequencies from 1 Hz to 500 Hz and established that the periodicity of the patterns reveals a strong dependence on the frequency of the applied AC field. Indeed, for 1 Hz, the macroscopic pattern can be observed even by the naked eye, as presented in Fig. S3. With the frequency change, a defect movement and reconfiguration took place with the consequent formation of a new pattern. For higher frequencies, the number of defects increased and the distance between them decreased. And *vice versa*, with the change from higher frequencies to lower, the distance between the defects increases. In the SI, the videos presenting the pattern structure changes with frequency are presented. For higher frequencies, the pattern reconfiguration was slower, which might relate to a larger number of defects and, hence, higher deformation energy of the system. The periodicity of the patterns induced by 100 Hz and 200 Hz applied fields practically did not differ. For frequencies higher than 200 Hz, the textures became massed and lacked any periodic features distinguishable by the POM. The pattern periodicity did not depend on temperature, at which it was induced, but at lower temperatures, the molecular reorientation was slower, and the periodic structure was generated after a longer time, reaching tens of seconds at RT. We have not found relevance between the amplitude of the applied field and the periodicity of the defects. The threshold field of the effect has been established to be about 1 V μm^{-1}. For lower field values, we observed only the director reorientation and the texture "flipping" as a response to the AC electric field, but no regular pattern generation.

We discovered that under the AC field application, we can induce a pseudo 2D square-lattice system of defects. By analogy

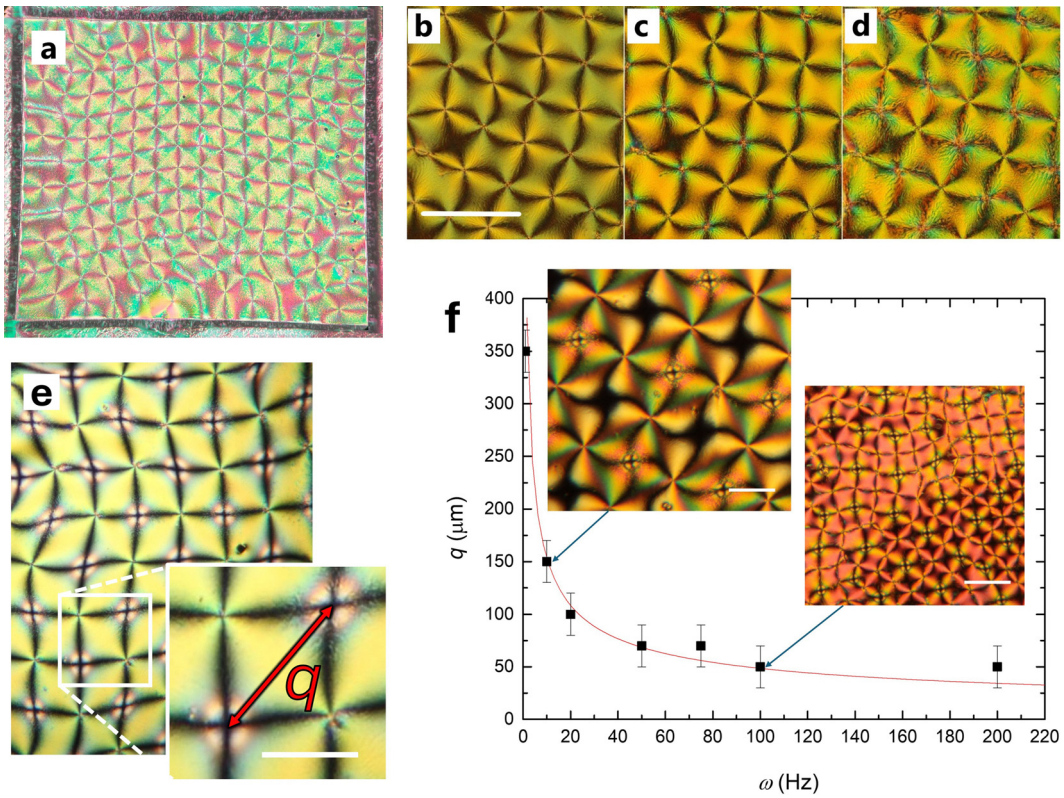

Fig. 1 Square-lattice patterns observed for a 5-μm HT sample in the N_F phase under the influence of an AC electric field: (a) POM image, taken at RT, of the 2D square-lattice system of defects covering the whole electrode area with the observed inhomogeneities close to the electrode edges, after the application of a 1 Hz AC electric field. The size of the electrode area is 5 mm × 5 mm. The crossed polarizer and analyzer are oriented along the edges of the photograph. Microphotographs taken at T = 40 °C: (b) under the applied AC electric field of 100 Hz, (c) immediately after and (d) 20 seconds after the field was switched off. (e) The pattern obtained using a 10 Hz AC field. Two types of defects are observed, switchable (upper right and bottom left in the inset) and unswitchable (upper left and bottom right in the inset). The mean distance between the defects of similar type, q, is shown in the inset. (f) The dependence of q on the frequency of the applied electric field, ω. The points are experimentally measured values, while the curve corresponds to the fitting of eqn (9). Additionally, the pattern textures obtained for certain frequency values are presented in the insets. The crossed polarizer and analyzer are along the edges of the photographs. The scale bar corresponds to 100 μm.

with ordinary nematics,[39] we can describe such a type of defect structure as a system of (±2π)-wedge disclinations. During the microscopic investigation of the patterns under the applied field, we observed that the defects are not all equal and two types of defects are present, differing in their response to the applied field. The difference is clearly visible for slower frequencies, and it consists in the fact that one type of defects is changing under the applied AC field, while the other type remains unchanged (see, for example, Video S2 in the SI). We will call the first type switchable defects, and the second one unswitchable defects. In Fig. 1(e), the pattern created using a 10 Hz applied field is presented. At this frequency, the difference between the above-mentioned defects is visible. In the inset of Fig. 1(e), an enlarged fragment of the pattern showing one unit cell of the structure is highlighted. In the upper right and bottom left corners of the square unit cell, the switchable defects are situated; subsequently, unswitchable defects are observed in the upper left and bottom right corners. The reason for the different defect behaviour and the nature of the defects will be speculated later in the Defect description and theoretical explanation section. It should be also mentioned that, as it is seen from Video S2 in the SI, the neighbouring switchable defects are switching out of phase, which will also be explained in the Defect description and theoretical explanation section.

We marked the distance between two neighbouring defects of the same type (switchable or unswitchable) as q (see the inset of Fig. 1(e)), with the aim of quantitatively describing the observed dependence of the pattern periodicity on the applied field frequency, ω. We established q for the patterns obtained at different values of ω, and the results of the measurements are presented in Fig. 1(f) (points with error bars). Based on the domain orientation under the polarized light microscope, the director profile of the pattern structure can be deduced. The domain orientation indicated the radial director distribution near the defects. To prove it, we acquired images with the full-wave retardation plate (λ-plate) and the quarter-wave retardation plate (λ/4-plate, changing the light polarization state into circular) inserted at 45°, λ = 530 nm (Fig. 2). The retardation plates allowed us to distinguish between the regions with different molecular orientations by the colour change.

Additionally, we studied the effect of the cell thickness on the defect array formation. Except for the previously studied

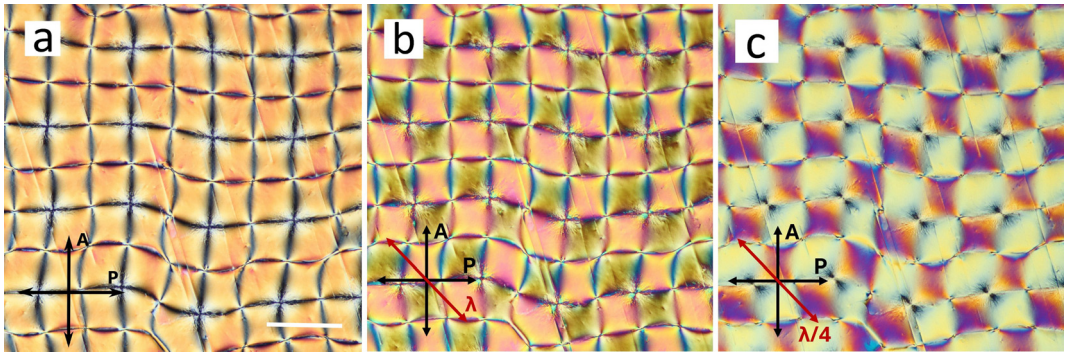

Fig. 2 POM images of the pattern structure generated by the 50 Hz AC electric field in the studied sample. The image obtained (a) without additional optical systems, (b) with a full-wave retardation plate (λ-plate) inserted at 45°, (c) with a quarter-wave retardation plate inserted at 45°. The polarizer and the analyzer are oriented along the edges of the photographs and are shown with black arrows; the retardation plates are shown with red arrows. The scale bar corresponds to 100 μm.

5-μm cell, we examined various thicknesses: 1.5, 3, 7 and 12 μm. For 3-μm and 7-μm cells, the texture behaviour resembled that described above for the 5-μm cell, with analogous parameters. However, for the 3-μm cell, the pattern formation process was slower and regular patterns appeared after longer periods of time than for the thicker cells, at least for tens of seconds. For the thin 1.5-μm cell, the pattern formation was strongly clamped by the cell surface influence, and the array of defects was not uniform.

Furthermore, we examined the effect of the AC field in other cell geometries, namely, for planar cells with antiparallel rubbing at the surfaces and for home-made glass cells without any surfactant layer. The virgin textures in planar antiparallel cells contained twisted domains (Fig. S4), as it was described in the previous study.[40] In this geometry, the applied electric field should overcome the surface anchoring and reorient the molecules at the surfaces. As in the N_F phase due to very high responsiveness to an electric field, the molecules could be easily reoriented,[35] the virgin homogeneous geometry was transformed into the homeotropic one by the applied voltage. Under an AC field, for the cells of thickness 3 μm and higher, we succeeded in creating similar defect patterns as in the homeotropic cells. For the thin 1.5-μm HG cell, the threshold field for the 2D square pattern creation increased up to 2.5 V μm^{-1}, and the pattern was not regular (Fig. S5). For the smaller field of 1–2.5 V μm^{-1}, stripe textures were observed perpendicular to the rubbing direction (Fig. S6) for frequencies 10 Hz and higher. At a small frequency of 1 Hz, any periodic features were not observed even for the field higher than 2.5 V μm^{-1}. Apparently, for the thin 1.5-μm planar cell, the influence of the surfaces dominated. The situation with the cells without any surfactant resembled the one described for homogeneous geometry, and the regular defect arrays were also generated.

2.1. Defect description and theoretical explanation

To elucidate the effect of the applied electric field in the ferroelectric N_F phase, let us point out the differences between the N_F phase and ordinary nematics relevant to the molecular organization at the sample surfaces. Due to the polarity of the molecules, there are different interactions of the molecular heads and tails with the surfactant layers.[41] While in ordinary nematics, the director configurations in aligned cells can be uniform, in the N_F phase, an additional twist (in planar cells with an antiparallel alignment) or splay (cells with homeotropic boundary conditions) will appear due to polar surface anchoring.

We suppose that the electric energy applied to the sample is transformed in the system, resulting in the creation of an array of defects. Additionally, defects can vibrate due to the interaction of the applied electric field with the spontaneous molecular polarization and the molecular reorientation brings about bound charges within the sample bulk. In general, the system of defects is unstable, but it is stabilised by an applied electric field.

In Fig. 3(a), we present the texture of the sample in the 5-μm HT cell under the applied field of frequency 10 Hz, augmented with the schematic expected director orientation shown by arrows, and, consequently, the molecular dipole moment arrangement. We consider that switchable defects are $(+2\pi)$-disclinations, with either positive or negative electric charge (red or blue points in Fig. 3(a)); unswitchable defects correspond to (-2π)-disclinations, and they are electrically not charged and are shown with white points.

The switching is related to the director reorganisation around the defects, and electrically charged defects compensate their charges at longer distances with their oppositely charged neighbours. Based on our observations, we can propose a schematic molecular orientation within the cell thickness for the electrically charged defects, shown in Fig. 3(b). Coordinate axes are chosen with the (x,y)-plane parallel to the surfaces and the z-axis across the sample. Parameter q is the mean distance between the neighbouring oppositely charged defects. The core regions of the electrically charged defects are along $(\pm z)$-directions with singular points (red and blue points) within the defects. The electrically charged defect length is marked as l_z (vertical dashed lines in Fig. 3(b)). We suppose that the electrically charged defects vibrate along the $(\pm z)$ direction,

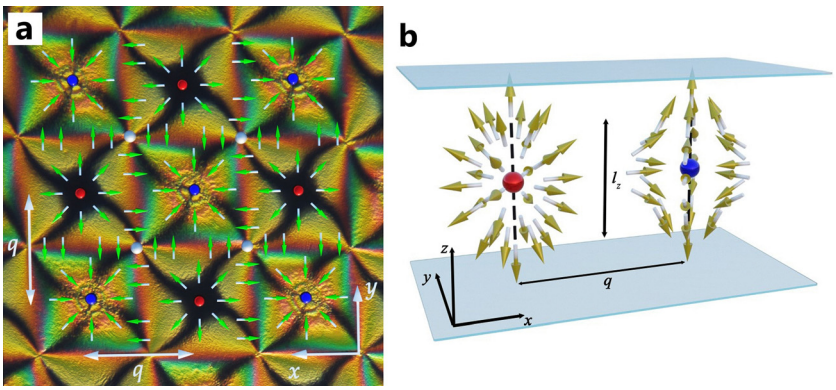

Fig. 3 Defect structures: (a) the texture of the sample in the 5-μm HT cell under the applied field of frequency 10 Hz and the schematic orientation of the molecules; arrows denote the molecular director and, consequently, the molecular dipole moment orientation. Coloured points are (+2π)-disclinations, while white points are (−2π)-disclinations. Evidently, (−2π)-disclinations are uncharged, while (+2π)-disclinations have either positive (red points), or negative (blue points) electric charges. (b) Schematic molecular orientation near the electrically charged defects in the sample with the HT polar anchoring geometry. Parameter q is the mean distance between the neighbouring oppositely charged defects, and the electrically charged defect length is marked as l_z.

while the vibration of the uncharged defects is negligible. The dynamics of the molecular reorganisation around the defects in response to the applied AC electric field is visualised in Video S4 and Video S5 in the SI. The video animations schematically demonstrate the vibrations of the electrically charged defects (Video S4) and only slight "antiphase" reorientation of the molecules in the vicinity of the uncharged ones (Video S5).

When an external AC electric field with frequency ω and amplitude E_0 is applied along the normal to the sample surfaces, it interacts with the spontaneous polarisation $\overrightarrow{P_S}$. The electric energy stimulates the creation of the defect system and its stabilisation. The electrically charged defects vibrate between the upper and lower glass plates along the z-axis (Fig. 3b) with the time dependent velocity $v = \dot{z}$. If we consider Φ to be the dissipated energy per unit time and take the defect density $\frac{1}{q^2}$, Φ can be written as $\Phi = -F_S v$ with the friction force $F_S = -\pi l_z \gamma_1 \ln\frac{R}{r_c} v$, which was calculated for the nematic phase in the literature.[42] Here R is the outer radius of the surface surrounding the disclination, r_c is the core radius, and parameter γ_1 is the nematic rotational viscosity. The force corresponding to the electric field interaction with the liquid crystal polarization can be written in the form of $-(\pi R^2)(P_S E_0 \cos\alpha_s)\cos(\omega t)$, where (πR^2) is the disclination area in the (x,y)-plane. We take α_s as a geometrical factor to describe the mean molecular inclination over the defect length l_z. We can expect that, in general, l_z depends on the frequency of the applied field. Nevertheless, for the simplicity of calculations, we consider it to be constant in the model. The energy of the electric field applied to the sample leads to the creation and stabilisation of the defect system due to the dissipation of the electric energy. In a stationary state, the energy balance between the field energy dissipated in the system per period $\tau = \frac{2\pi}{\omega}$ and the disclination self-energy, E_S, multiplied by the defect density, will be in equilibrium with the energy of the electric field:

$$\frac{1}{q^2}\left[\int_0^\tau \Phi \mathrm{d}t + E_S\right] = \frac{1}{\tau}\int_0^\tau |hP_S E_0 \cos\alpha_s \cos(\omega t)|\mathrm{d}t \qquad (1)$$

The total disclination self-energy of the charged disclinations, E_S, consists of the elastic energy, E_{es}, and the electric contribution, E_Q:

$$E_S = E_{es} + E_Q \qquad (2)$$

The elastic energy of the disclinations can be written in a form described in the literature for nematics:[7,42]

$$E_{es} = l_z \pi K \ln\frac{R}{r_c} \qquad (3)$$

where K is the elastic constant in one-constant approximation. To estimate the electric interactions of the electrically charged defects in the sample, the disclination self-energy due to the disclination charge can be expressed in an analogous way to the one described in the literature for classical electrodynamics:[43]

$$E_Q = \frac{1}{2\varepsilon_0\varepsilon_r}\int\int\frac{\rho(\vec{r})\rho(\vec{r}')}{|\vec{r}-\vec{r}'|}\mathrm{d}V\mathrm{d}V' \approx \frac{Q^2}{2\varepsilon_0\varepsilon_r l_z^2}\int_{-\frac{l_z}{2}}^{\frac{l_z}{2}}\mathrm{d}z\int_{-\frac{l_z}{2}}^{\frac{l_z}{2}}\mathrm{d}z'\frac{1}{\sqrt{r_c^2+(z-z')^2}} \qquad (4)$$

where ε_0 and ε_r are the dielectric permittivity of vacuum and the relative permittivity, respectively. The volume density of charges $\rho(\vec{r})$ is Q/V, where the volume V contains one disclination, *i.e.* $V \sim \pi R^2 l_z$. Configurational disclination charge Q can be determined as $Q \approx \pi(R - r_c) l_z P_S \sin\alpha_s$, as it was described for the disclinations in ferroelectric smectics.[44] As $l_z > r_c$, the above double integral can be evaluated as $\sim l_z \ln\frac{l_z}{r_c}$ and the self-energy of the electrically charged disclination of length l_z can be

estimated as $E_Q = \frac{Q^2}{2\varepsilon_0\varepsilon_r l_z}\ln\frac{l_z}{r_c}$. We take the following expression as the approximated total disclination self-energy:

$$E_S = l_z \pi K \ln\frac{R}{r_c} + \frac{Q^2}{2\varepsilon_0\varepsilon_r l_z}\ln\frac{l_z}{r_c} \quad (5)$$

To obtain the dynamic equation, we may introduce the temporary force $-\pi l_z \gamma_1 \ln\frac{R}{r_c}\dot{z}$ and the dynamical equation takes the following form:

$$-l_z\pi\gamma_1 \ln\frac{R}{r_c}\dot{z} - \left(\pi R^2\right)(P_S E_0 \cos\alpha_s)\cos(\omega t) = 0 \quad (6)$$

We expect that the electrically charged defect follows the electric field frequency and eqn (6) gives the velocity $\dot{z}$ of the disclination vibration. The expression $\int_0^\tau \Phi \mathrm{d}t$ can be then evaluated as

$$\int_0^\tau \Phi \mathrm{d}t = \pi l_z \gamma_1 \ln\frac{R}{r_c}\cdot\int_0^\tau (\dot{z})^2 \mathrm{d}t = \frac{\pi}{\omega}\frac{\left(\pi R^2\right)^2 (P_S E_0 \cos\alpha_s)^2}{\left(\pi l_z \gamma_1 \ln\frac{R}{r_c}\right)} \quad (7)$$

One can find the detailed calculations in the SI. From the calculations, the obtained distance between the defects is

$$q(\omega) = \sqrt{\frac{\pi}{2}}\sqrt{\frac{\left(\pi R^2\right)^2 (P_S E_0 \cos\alpha_s)}{\omega h l_z \gamma_1 \ln\frac{R}{r_c}} + \frac{E_S}{h(P_S E_0 \cos\alpha_s)}} \quad (8)$$

We simplified such a dependence on the applied field frequency to the following expression:

$$q = \sqrt{\frac{a}{\omega} + b} \quad (9)$$

and fitted to this equation the experimental data demonstrated in Fig. 1(f) (red curve). This frequency characteristic reflects the fact that at higher frequencies, the defects cannot follow the oscillations of the applied field.

3. Discussion and conclusions

In this research, we demonstrate the controlled induction of topological defect arrays in a ferroelectric nematic liquid crystal confined in sandwich-type cells with a homeotropic surface molecular alignment, without employing any surface pre-patterning. The defect structures are generated under the application of a low frequency alternating electric field. Experimental conditions and parameters characterizing the resulting defect patterns have been systematically established.

We propose that the applied electric energy is transformed in the LC medium, leading to the formation of both electrically charged and uncharged defects in the system. The observed defect structures are $(\pm 2\pi)$-disclinations. Under the influence of the alternating electric field, the electrically charged defects exhibit oscillatory motion along the z-axis, perpendicular to the cell substrates. In contrast, the uncharged defects remain stationary, accompanied only by local molecular reorientation, and their self-energy is of elastic origin. On the other hand, the self-energy of the electrically charged defects additionally includes the electrical charge energy and the vibrational component. Given the large inter-defect spacing on the order of hundreds of micrometres, mutual interaction energies between the defects can be considered negligible.

We consider that there is a balance between electrostatic and elastic energies of the defect pattern and the energy transferred from the oscillating electric field. The reason for the periodic array could lie in the frustration of the system due to polar anchoring conditions and the orientation of an applied electric field. As a result of the director deformations, a 2D periodic lattice of defects forms to minimize their interaction energy.

We infer that the induced defect arrays exhibit zero total polarization, as local molecular dipole moments are mutually compensated within the periodic structure. To elucidate the underlying mechanism, we developed a theoretical model describing the system's dynamic equilibrium and derived the dependence of the defect structure parameter, the distance between the defects, q, on the frequency of the applied AC field. The experimental data were fitted to the obtained dependence, revealing a good consistency despite the model simplifications (Fig. 1(f)). The extracted fitting parameters were analysed in the context of material properties. Notably, the nematic rotational viscosity, γ_1, derived from the fitting procedure for the studied N_F compound NF6 was found to be approximately an order of magnitude higher than typical values reported for conventional nematics.[42] We attribute this high viscosity value to the fact that the effect for the NF6 compound was observed at room temperature, where the material viscosity naturally increases, and propose that high material viscosity plays a crucial role in enabling the observed defect formation dynamics.

In the proposed energy balance, the defect self-energies and the dissipative energies are the terms principally transforming the energy input from the applied oscillating field. This framework offers an original approach for interpreting field-induced self-organizing phenomena, with potential applicability across a broader class of soft matter and biologically relevant systems.

The concept of active matter is relevant to systems maintained out of thermodynamic equilibrium through continuous energy input.[45] It provides a useful lens for interpreting our results as through the transformation of the applied electric field energy, the system self-arranges into the quasi-equilibrium defect array structure. In active nematics,[46] topological defects are generated and annihilated, bringing about new functionalities. Most often, the observed topological defects appear chaotically. In contrast, the ferroelectric nematic system investigated here exhibits a stable, reconfigurable defect lattice. This controllable response, governed by the interplay of material elasticity and polar responsiveness to external fields, suggests new avenues for functional soft-matter design. These findings might offer opportunities for the development of tunable platforms for emerging technologies, including adaptive optics and soft robotics.

4. Methods

For our research, we utilised ferroelectric nematic liquid crystalline compound NF6, the synthesis and mesomorphic properties of which were published previously.[15] We used sandwich-type commercial glass cells, purchased from the WAT PPW company, Poland, with transparent indium tin oxide (ITO) electrodes and surfactant layers ensuring homeotropic (HT) or homogeneous (HG) geometries. Various cell thicknesses of 1.5, 3, 5, 7 and 12 μm were used to investigate the dependence of the obtained structures on the cell gap. The electrode area of the cells was 25 mm^2 for all of the samples. Besides, a cell with a larger electrode area (64 mm^2) was utilised for comparison.

The cells were filled with the material in the isotropic (Iso) phase by means of capillary action. The textures were investigated under the polarizing light microscope Nikon Eclipse E600, equipped with a Linkam heating–cooling stage with temperature stabilisation of ±0.1 K and a temperature controller Linkam TMS 94. A Canon EOS 700D camera was used for texture photograph and video acquisition.

Author contributions

V. N. supervised the project; N. P. conducted the experimental work and data analysis; L. L. developed the theoretical model and carried out the calculations; M. C. is responsible for the materials studied; N. P., V. N. and L. L. prepared the manuscript.

Conflicts of interest

The authors declare that they have no competing interests.

Data availability

Data relevant to this study can be found in the SI. SI contains additional photographs of the textures and cells and detailed theoretical calculations. Additionally, video files showing patterns reconfiguration and animated molecular reorganization near the defects of different types are provided. See DOI: **https://doi.org/10.1039/d5sm00747j**.

Additional information can be provided by the corresponding author upon request.

Acknowledgements

The authors acknowledge the project 24-10247K (the Czech Science Foundation).

References

1 M. A. N. Araujo and P. D. Sacramento. *Topology in Condensed Matter: An Introduction*, World Scientific, Singapore, 2021.
2 M. J. Gilbert, Topological electronics, *Commun. Phys.*, 2021, **4**, 70.
3 K.-H. Jin, W. Jiang, G. Sethi and F. Liu, Topological quantum devices: a review, *Nanoscale*, 2023, **31**, 12787–12817.
4 J. Peng, R.-Y. Zhang, S. Jia, W. Liu and S. Wang, Topological near fields generated by topological structures, *Sci. Adv.*, 2022, **8**, eabq0910.
5 F. Serra, U. Tkalec and T. Lopez-Leon, Editorial: topological soft matter, *Front. Phys.*, 2020, **8**, 373.
6 L. Tubiana, G. P. Alexander, A. Barbensi, D. Buck, J. H. E. Cartwright, M. Chwastyk, M. Cieplak, I. Coluzza, S. Čopar, D. J. Craik, M. Di Stefano, R. Everaers, P. F. N. Faísca, F. Ferrari, A. Giacometti, D. Goundaroulis, E. Haglund, Y.-M. Hou, N. Ilieva, S. E. Jackson, A. Japaridze, N. Kaplan, A. R. Klotz, H. Li, C. N. Likos, E. Locatelli, T. Lopez-Leon, T. Machon, C. Micheletti, D. Michieletto, A. Niemi, W. Niemyska, S. Niewieczerzal, F. Nitti, E. Orlandini, S. Pasquali, A. P. Perlinska, R. Podgornik, R. Potestio, N. M. Pugno, M. Ravnik, R. Ricca, C. M. Rohwer, A. Rosa, J. Smrek, A. Souslov, A. Stasiak, D. Steer, J. Sulkowska, P. Sulkowski, D. W. L. Sumners, C. Svaneborg, P. Szymczak, T. Tarenzi, R. Travasso, P. Virnau, D. Vlassopoulos, P. Ziherl and S. Žumer, Topology in soft and biological matter, *Phys. Rep.*, 2024, **1075**, 1–137.
7 P. G. De Gennes and J. Prost, *The Physics of Liquid Crystals*, Clarendon Press, Oxford, 1995.
8 N. V. Madhusudana and K. R. Sumathy, Observations on a nematic liquid crystal with an oblique orientation of the director at the nematic-isotropic interface, *Mol. Cryst. Liq. Cryst.*, 1985, **129**, 137–147.
9 Q. Zhang, W. Wang, S. Zhou, R. Zhang and I. Bischofberger, Flow-induced periodic chiral structures in an achiral nematic liquid crystal, *Nat. Commun.*, 2023, **15**, 7.
10 A. Buka and L. Kramer. *Pattern Formation in Liquid Crystals*, Springer, New York, 1996.
11 N. Eber, P. Salamon and A. Buka, Electrically induced patterns in nematic and how to avoid them, *Liq. Cryst. Rev.*, 2016, **4**, 101–134.
12 B.-X. Li, R.-L. Xiao, S. Paladugu, S. V. Shiyanovskii and O. D. Lavrentovich, Three-dimensional solitary waves with electrically tunable direction of propagation in nematics, *Nat. Commun.*, 2019, **10**, 3749.
13 Y. Sasaki, Y. V. S. R. Jampani, C. Tanaka, N. Sakurai, S. Sakane, K. V. Le, F. Araoka and H. Orihara, Large-scale self-organization of reconfigurable topological defect networks in nematic liquid crystals, *Nat. Commun.*, 2016, **7**, 13238.
14 M. Kim and F. Serra, Tunable dynamic topological defect pattern formation in nematic liquid crystals, *Adv. Opt. Mater.*, 2020, **8**, 1900991.
15 M. Wang, Y. Li and H. Yokoyama, Artificial web of disclination lines in nematic liquid crystals, *Nat. Commun.*, 2017, **8**, 388.
16 R. J. Mandle, S. J. Cowling and J. W. Goodby, A nematic to nematic transformation exhibited by a rod-like liquid crystal, *Phys. Chem. Chem. Phys.*, 2017, **19**, 11429–11435.
17 H. Nishikawa, K. Shiroshita, H. Higuchi, Y. Okumura, Y. Haseba, S. Yamamoto, K. Sago and H. Kikuchi, A fluid

liquid-crystal material with highly polar order, *Adv. Mater.*, 2017, **29**, 1702354.
18 R. J. Mandle, S. J. Cowling and J. W. Goodby, Rational design of rod-like liquid crystals exhibiting two nematic phases, *Chem. – Eur. J.*, 2017, **23**, 14554–14562.
19 M. Born, Über anisotrope Flüssigkeiten. Versuch einer Theorie der flossing Kristalle und des elektrischen Kerr-Effekts in Flüssigkeiten, *Ann. Phys.*, 1918, **55**, 221.
20 O. D. Lavrentovich, Ferroelectric nematic liquid crystal, a century in waiting, *Proc. Natl. Acad. Sci. U. S. A.*, 2020, **117**, 14629–14631.
21 R. J. Mandle, N. Sebastian, J. Martinez-Perdiguero and A. Mertelj, On the molecular origins of the ferroelectric splay nematic phase, *Nat. Commun.*, 2021, **12**, 4962.
22 J. X. Li, H. Nishikawa, J. Kougo, J. Zhou, S. Dai, W. Tang, X. Zhao, Y. Hisai, M. J. Huang and S. Aya, Development of ferroelectric nematic fluids with giant dielectricity and nonlinear optical properties, *Sci. Adv.*, 2021, **7**, eabf5047.
23 R. J. Mandle, S. J. Cowling and J. W. Goodby, Structural variants of RM734 in the design of splay nematic materials, *Liq. Cryst.*, 2021, **48**, 1780–1790.
24 M. Cigl, N. Podoliak, T. Landovský, D. Repček, P. Kužel and V. Novotná, Giant permittivity in dimethylamino-terminated ferroelectric nematogens, *J. Mol. Liq.*, 2023, **385**, 122360.
25 R. Saha, P. Nepal, C. Feng, M. S. Hossain, M. Fukuto, R. Li, J. T. Gleeson, S. Sprunt, R. J. Twieg and A. Jakli, Multiple ferroelectric nematic phases of a highly polar liquid crystal compound, *Liq. Cryst.*, 2022, **49**, 1784–1796.
26 A. Manabe, M. Bremer and M. Kraska, Ferroelectric nematic phase at and below room temperature, *Liq. Cryst.*, 2021, **48**, 1079–1086.
27 S. Brown, E. Cruickshank, J. M. D. Storey, C. T. Imrie, D. Pociecha, M. Majewska, A. Makal and E. Gorecka, Multiple polar and non-polar nematic phases, *ChemPhysChem*, 2021, **22**, 2506–2510.
28 Y. Song, J. Li, R. Xia, H. Xu, X. Zhang, H. Lei, W. Peng, S. Dai, S. Aya and M. Huang, Development of emergent ferroelectric nematic liquid crystals with highly fluorinated and rigid mesogens, *Phys. Chem. Chem. Phys.*, 2022, **24**, 11536–11543.
29 J. Karcz, N. Rychlowicz, M. Czarnecka, A. Kocot, J. Herman and P. Kula, Enantiotropic ferroelectric nematic phase in a single compound, *Chem. Commun.*, 2023, **25**, 14807–14810.
30 G. Stefanafas, E. Cruickshank, S. Brown, M. M. Majewska, D. Pociecha, E. Gorecka, J. M. D. Storey and C. T. Imrie, Ferroelectric nematogens containing a methylthio group, *Mater. Adv.*, 2024, **5**, 525–538.
31 M. Mrukiewicz, M. Czerwinski, N. Podoliak., D. Repček, P. Perkowski, R. J. Mandle and D. Weglowska, Polar nematic phases with enantiotropic ferro- and antiferroelectric behavior, *J. Mater. Chem. C*, 2024, **12**, 7214–7224.
32 N. Sebastian, M. Copic and A. Mertelj, Ferroelectric nematic liquid-crystalline phases, *Phys. Rev. E*, 2022, **106**, 021001.
33 H. Nishikawa, K. Sano and F. Araoka, Anisotropic fluid with phototunable dielectric permittivity, *Nat. Commun.*, 2022, **13**, 1142.
34 N. Sebastian, R. J. Mandle, A. Petelin, A. Eremin and A. Mertelj, Electrooptics of mm-scale polar domains in the ferroelectric nematic phase, *Liq. Cryst.*, 2021, **48**, 2055–2071.
35 X. Chen, E. Korblova, D. Dong, X. Wei, R. Shao, L. Radzihovsky, M. A. Glaser, J. E. Maclennan, D. Bedrov, D. M. Walba and N. A. Clark, First-principles experimental demonstration of ferroelectricity in a thermotropic nematic liquid crystal: Polar domains and striking electro-optics, *Proc. Natl. Acad. Sci. U. S. A.*, 2020, **117**, 14021–14031.
36 X. Chen, E. Korblova, M. A. Glaser, J. E. Maclennan, D. M. Walba and N. A. Clark, Polar in-plane surface orientation of a ferroelectric nematic liquid crystal: Polar monodomains and twisted state electro-optics, *Proc. Natl. Acad. Sci. U. S. A.*, 2021, **118**, 2104092118.
37 N. Sebastian, M. Lovšin, B. Berteloot, N. Osterman, A. Petelin, R. J. Mandle, S. Aya, M. Huang, I. Drevenšek-Olenik, K. Neyts and A. Mertelj, Polarization patterning in ferroelectric nematic liquids via flexoelectric coupling, *Nat. Commun.*, 2023, **14**, 3029.
38 B. Basnet, S. Paladugu, O. Kurochkin, O. Buluy, N. Aryasova, V. G. Nazarenko, S. V. Shiyanovskii and O. D. Lavrentovich, Periodic splay Freedericksz transitions in a ferroelectric nematic, *Nat. Commun.*, 2025, **16**, 1444.
39 S.-B. Wu, J.-B. Wu, H.-M. Cao, Y.-Q. Lu and W. Hu, Topological defect guided order evolution across the nematic-smectic phase transition, *Phys. Rev. Lett.*, 2023, **130**, 078101.
40 V. Novotná, L. Lejček and N. Podoliak, Twisted domains in ferroelectric nematic liquid crystals, *J. Mol. Liq.*, 2024, **403**, 124873.
41 F. Caimi, G. Nava, R. Barboza, N. A. Clark, E. Korblova, D. M. Walba, T. Bellini and L. Lucchetti, Surface alignment of ferroelectric nematic liquid crystals, *Soft Matter*, 2021, **17**, 8130–8139.
42 P. Ostwald and P. Pieranski. *Nematic and Cholesteric Liquid Crystals*, Taylor and Francis, Boca Raton, 2005.
43 J. D. Jackson. *Classical Electrodynamics*, J. Wiley and Sons, New York, 1963.
44 L. Lejček, Twist disclinations in ferroelectric liquid crystals as sources of induced polarization space charges, *Ferroelectrics*, 2002, **278**, 21–28.
45 R. Zhang, A. Mozaffari and J. J. de Pablo, Autonomous materials systems from active liquid crystals, *Nat. Rev. Mater.*, 2021, **6**, 437–453.
46 A. Doostmohammadi, J. Ignes-Mullon, J. M. Yeomans and F. Sagues, Active nematics, *Nat. Commun.*, 2018, **9**, 3246.

